

CNOT gates for fluxonium qubits via selective darkening of transitions

Konstantin N. Nesterov,^{1,2,*} Chen Wang,³ Vladimir E. Manucharyan,⁴ and Maxim G. Vavilov¹

¹*Department of Physics and Wisconsin Quantum Institute,
University of Wisconsin-Madison, Madison, WI 53706, USA*

²*Bleximo Corp., Berkeley, CA 94710, USA*

³*Department of Physics, University of Massachusetts-Amherst, Amherst, MA, 01003, USA*

⁴*Department of Physics, University of Maryland, College Park, MD 20742, USA*

(Dated: September 27, 2022)

We analyze the cross-resonance effect for fluxonium circuits and investigate a two-qubit gate scheme based on selective darkening of a transition. In this approach, two microwave pulses at the frequency of the target qubit are applied simultaneously with a proper ratio between their amplitudes to achieve a controlled-NOT operation. We study in detail coherent gate dynamics and calculate gate error. With nonunitary effects accounted for, we demonstrate that gate error below 10^{-4} is possible for realistic hardware parameters. This number is facilitated by long coherence times of computational transitions and strong anharmonicity of fluxoniums, which easily prevents excitation to higher excited states during the gate microwave drive.

I. INTRODUCTION

Two-qubit gates with very low error rates are essential for making a practical quantum processor. In superconducting architectures [1–3], such operations with fidelity approaching 99.9% have already been demonstrated [4–7]. In the family of two-qubit gates utilizing microwave control, one of the most successful and popular gate schemes is based on the cross-resonance (CR) effect, which results in the controlled-NOT (CNOT) operation up to local single-qubit rotations [8, 9]. This gate is activated by driving the control qubit at the frequency of the target qubit (CR drive). It has been implemented experimentally multiple times, including experiments with ordinary flux qubits [10], capacitively shunted flux qubits [11], and transmons [5, 7, 12–16]. These experiments are accompanied by several theoretical publications that discuss the gate and techniques of its improvement in great detail [17–23].

Despite being a common superconducting qubit, the transmon has a drawback of having a weakly anharmonic energy spectrum, which generally complicates qubit control. A promising alternative to the transmon is the fluxonium circuit with its strongly anharmonic spectrum and long coherence time of the low-frequency transition between the ground and first excited states [24–26]. One of the microwave-activated two-qubit gate schemes that has been implemented experimentally with fluxonium qubits is based on driving in proximity with transitions leading to higher (noncomputational) excited states of the two-qubit spectrum [27, 28]. Such gate operations are facilitated by several-gigahertz transmon-like frequencies of those transitions, which results in stronger interactions between noncomputational levels in comparison to interactions between computational levels [29]. A gate scheme based on populating higher excited states was also sug-

gested for heavy fluxoniums [30]. To fully benefit from a long coherence time of the main qubit transitions of fluxoniums, the population, however, should remain in the computational subspace during the gate operation. This reasoning has been used in a recent proposal of a two-qubit gate based on activating a two-photon transition by a strong microwave drive [31]. Because the fluxonium spectrum is anharmonic, a strong drive amplitude in that proposal does not cause significant leakage to noncomputational levels, and gate fidelity is therefore not spoiled by shorter coherence times of higher excited states. Other methods to remain in the computational subspace are to implement flux-tunable gates [32–34] or tunable couplers [35], although these schemes may incur first-order flux noise and require added hardware complexity.

In this paper, we explore theoretically the CR gate for fluxoniums and therefore continue studying gate schemes that benefit in full from long coherence time of computational transitions. We focus on the selective-darkening (SD) variant of the CR gate, which was studied both experimentally [10] and theoretically [17] for flux qubits and has been lately used for transmons under the name of direct CNOT [5, 7, 16, 23]. In addition, more recently, the SD variant was demonstrated for fluxonium circuits [36]. In this scheme, a strong CR drive of the control qubit is accompanied by a weak drive of the target qubit that is chosen to cancel rotation of the target qubit when the control qubit is in its ground state. When the control qubit is in its excited state, the target qubit rotates, which, with proper calibration, results in CNOT operation. Using the language of effective Hamiltonian models [8, 20], these two tones result in effective ZX and IX terms of equal magnitudes but opposite signs. The primary effect of the CR drive without the second tone is to produce some unbalanced combination of ZX and IX terms, which requires an additional single-qubit rotation of the target qubit to achieve CNOT. This basic scheme can be improved by using an echo sequence of two CR drives of opposite signs and of additional π rotations of the control qubit, which eliminates various spurious

* konstantin@bleximo.com

terms in the effective Hamiltonian such as ZI and ZZ and makes the operation insensitive to the low-frequency amplitude noise [13–15, 21, 22].

Nevertheless, the SD approach, which produces a direct CNOT operation without using an echo sequence and additional single-qubit rotations, results in faster gates and has been demonstrated experimentally to work well for transmons [5, 7, 16]. We illustrate via simulations that such a scheme produces high-fidelity and fast gates for fluxoniums as well, which holds even when ZZ crosstalk is relatively strong. We show that this operation is facilitated by the structure of interaction matrix elements, which are enhanced for transitions to higher energy levels, eventually allowing one to achieve reasonably fast speeds for the proposed two-qubit gate. The operation requires single-qubit Z rotations, which can be done instantly in software [37]. For realistic fluxonium parameters with qubit lifetimes of 500 μs and 50 μs of the first and second excited states, we find greater than 99.99% coherent fidelity for gate duration of 50 ns without using any advanced pulse shaping. In experiment of Ref. [36], the gate error was shown to be about 0.5% with qubits having short coherence times in the range of 10-20 μs . The incoherent error is dominated by lifetime of the computational subspace: even when the relaxation time of the second excited states in simulations is only 1 μs , its contribution to this error is below 0.1%.

The outline of the paper is as follows. In Sec. II, we review the model of two coupled fluxoniums, the gate concept, discuss in detail the structure of charge matrix elements relevant for the gate operation, and elaborate on fundamental limitations on gate rate. In Sec. III, we discuss our simulations of the unitary dynamics, coherent error budget, and the reduction of gate fidelity by nonunitary processes. Finally, we conclude in Sec. IV.

II. MODEL AND GATE CONCEPT

A. Interacting fluxoniums

We consider the system of two capacitively coupled fluxonium circuits in the presence of two local microwave drives, which is shown schematically in Fig. 1(a). Without the loss of generality, we assume that qubits A and B are the control and target qubits, respectively, so the local drive applied to qubit A is the CR drive, whose amplitude is larger than the amplitude of the second drive. Both drives are applied at the same frequency $\omega_d \approx \omega_{01}^B$, where ω_{kl}^α is the frequency of the single-qubit transition $|k_\alpha\rangle - |l_\alpha\rangle$ between two eigenstates of qubit α ($\alpha = A, B$).

We model this system by the Hamiltonian

$$\hat{H} = \hat{H}_A^{(0)} + \hat{H}_B^{(0)} + \hat{V} + \hat{H}_{\text{drive}}, \quad (1)$$

where the first two terms describe individual qubits and are given by

$$\hat{H}_\alpha^{(0)} = 4E_{C,\alpha}\hat{n}_\alpha^2 + \frac{1}{2}E_{L,\alpha}\hat{\varphi}_\alpha^2 - E_{J,\alpha}\cos(\hat{\varphi}_\alpha - \phi_{\text{ext},\alpha}) \quad (2)$$

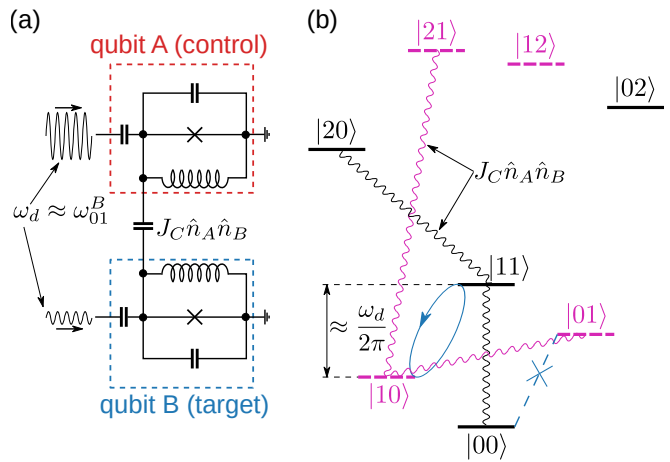


FIG. 1. Circuit diagram (a) and energy levels (b) of two capacitively coupled fluxonium qubits A and B driven by two local microwave fields with frequency ω_d . When $\omega_d \approx \omega_{01}^B$, a strong drive of qubit A and a properly chosen much weaker drive of qubit B realize a controlled- U gate operation on qubit B (target), so qubit B is rotated only when qubit A (control) is in $|1\rangle$. Wavy lines in panel (b) illustrate pairs of hybridized two-qubit levels that give dominant contributions to $\langle 10|\hat{n}_A|11\rangle$.

with $\alpha = A, B$. Here $\hat{\varphi}_\alpha$ and \hat{n}_α are the dimensionless position-like flux operator and momentum-like charge operator with the commutation relation $[\hat{\varphi}_\alpha, \hat{n}_{\alpha'}] = i\delta_{\alpha\alpha'}$. The third term in Eq. (2) describes capacitive interaction according to

$$\hat{V} = J_C \hat{n}_A \hat{n}_B. \quad (3)$$

Parameters of Eqs. (2) and (3) are discussed in detail in Refs. [29, 31]. Here we briefly note that each qubit is characterized by its charging ($E_{C,\alpha}$), inductive ($E_{L,\alpha}$), and Josephson ($E_{J,\alpha}$) energies as well as the dimensionless variable $\phi_{\text{ext},\alpha}$, which is proportional to the external magnetic flux threading the loop formed by the superinductor and Josephson junction. The value of $\phi_{\text{ext},\alpha}$ is tunable *in situ*, and, similarly to other microwave-activated schemes, here we consider fluxoniums permanently parked at their sweet spots of maximal coherence at $\phi_{\text{ext},\alpha} = \pi$ [25, 26]. The interaction strength J_C in Eq. (3) is determined by the mutual capacitance and individual capacitances of the two qubits [29, 31]. Finally, the last term in Eq. (1) describes the coupling to two external microwave drives of frequency ω_d :

$$\hat{H}_{\text{drive}} = 2\hbar f(t) \cos(\omega_d t) (\hat{n}_A + \eta \hat{n}_B). \quad (4)$$

Here $\hbar = h/2\pi$ is the reduced Planck constant, $f(t)$ is the time-dependent field envelope, and η captures the combined effect of different drive amplitudes and of classical crosstalk. We emphasize that because of this crosstalk in a realistic system, each local drive couples to both qubits, so η is not simply the ratio of two drive amplitudes. However, if the ratio of two amplitudes can be tuned, the value of η can be tuned as well.

B. Gate concept

An essential condition of any CR scheme is the dependence of the drive matrix element for target-qubit transitions on the state of the control qubit. Let $|kl\rangle$ be the dressed two-qubit eigenstate of Hamiltonian (1) at $\hat{H}_{\text{drive}} = 0$ corresponding to the noninteracting tensor-product state $|k_A\rangle|l_B\rangle$. Then, for our choice of the control and target qubits, each target-qubit transition is between states $|k0\rangle$ and $|k1\rangle$ for some k . Therefore, the essential CR condition implies

$$\langle 00|\hat{H}_{\text{drive}}|01\rangle \neq \langle 10|\hat{H}_{\text{drive}}|11\rangle. \quad (5)$$

This way, the Bloch-sphere trajectory of qubit B in the presence of $\hat{H}_{\text{drive}} \neq 0$ depends on the state of qubit A . When $J_C = 0$, we find that the inequality (5) is violated since both sides reduce to the same value determined by the single-qubit charge matrix element $\langle 0_B|\hat{n}_B|1_B\rangle$ for the target qubit. When $J_C \neq 0$, two-qubit bare states $|k_A\rangle|l_B\rangle$ hybridize to form dressed states $|kl\rangle$. Because of this hybridization, $\langle k0|\hat{H}_{\text{drive}}|k1\rangle$ acquires a k -dependent correction coming from corrections to both $\langle k0|\hat{n}_A|k1\rangle$ and $\langle k0|\hat{n}_B|k1\rangle$.

The SD condition requires one of the transition matrix elements of \hat{H}_{drive} to vanish. To be specific, we take

$$\langle 00|\hat{H}_{\text{drive}}|01\rangle = 0, \quad (6)$$

which, together with inequality (5), implies that only $|10\rangle - |11\rangle$ transition is activated, while $|00\rangle - |01\rangle$ transition is made forbidden, see Fig. 1(b). Using Eq. (4), we find that the SD condition (6) is equivalent to

$$\eta = -\frac{\langle 00|\hat{n}_A|01\rangle}{\langle 00|\hat{n}_B|01\rangle}. \quad (7)$$

The resonance Rabi frequency for the $|10\rangle - |11\rangle$ transition for the continuous drive $f(t) = \text{const.}$ in Eq. (4) is then given by

$$\Omega_{10-11} = 2f \left| \langle 10|\hat{n}_A|11\rangle - \langle 00|\hat{n}_A|01\rangle \frac{\langle 10|\hat{n}_B|11\rangle}{\langle 00|\hat{n}_B|01\rangle} \right|. \quad (8)$$

The CNOT gate duration is given by half period of Rabi oscillations: $t_{\text{gate}} = \pi/\Omega_{10-11}$.

We further refer to the two-qubit charge matrix elements of the type $\langle k0|\hat{n}_A|k1\rangle$ as cross matrix elements; they are zero at $J_C = 0$. Matrix elements of the second type, $\langle k0|\hat{n}_B|k1\rangle$, are referred to as direct matrix elements; they reduce to single-qubit values at $J_C = 0$. The first nonvanishing correction to the cross matrix elements is linear in J_C , while it is only quadratic for the direct matrix elements because of the parity selection rules for the charge operators at half flux quantum [29, 31]. Therefore, to linear order in J_C , we find

$$\Omega_{10-11} = 2f |\langle 10|\hat{n}_A|11\rangle - \langle 00|\hat{n}_A|01\rangle| + O(J_C^2). \quad (9)$$

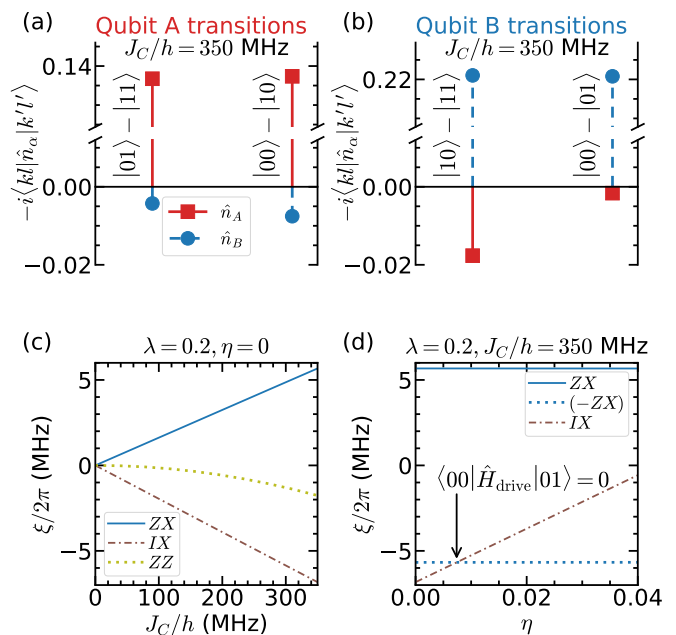


FIG. 2. (a), (b) Matrix elements of qubit charge operators \hat{n}_A (red squares) and \hat{n}_B (blue circles) for various computational transitions calculated for parameters of Table I at $J_C/h = 350$ MHz. The cross matrix elements, e.g., $\langle 10|\hat{n}_A|11\rangle$, give the dominant contribution to the CR effect. (c) The rates of effective ZX (blue solid line), IX (brown dash-dot line), and ZZ (cyan dotted line) interactions calculated using Eqs. (12a)-(12c) vs J_C for $\lambda = 0.2$ [see Eq. (13)] and $\eta = 0$. (d) The rates of ZX , negative ZX (blue dotted line), and IX interactions vs η at $\lambda = 0.2$ and $J_C/h = 350$ MHz.

By analogy, if qubit A is chosen as the target qubit and qubit B is the control, we find

$$\Omega_{01-11} = 2f |\langle 01|\hat{n}_B|11\rangle - \langle 00|\hat{n}_B|10\rangle| + O(J_C^2). \quad (10)$$

Therefore, to linear order in J_C , Rabi rates for the CR effect are determined by the cross matrix elements. We calculate the values of both cross and direct charge matrix elements in the next section.

C. Charge matrix elements

For quantitative analysis, we use realistic hardware parameters shown in Table I with variable interaction strength J_C . Single-qubit frequencies for these parameters are in the 500-1000 MHz range, which ensures that n_{01}^α , where $n_{kl}^\alpha = -i\langle k_\alpha|\hat{n}_\alpha|l_\alpha\rangle$, is not very small to allow a sufficient hybridization of computational levels with relevant states both inside and outside of the computational subspace. In comparison, devices with single-qubit transition frequencies in the 100-200 MHz range result in $n_{01}^\alpha \lesssim 0.05$, making gate operations based on hybridization of computational levels more challenging to implement. Such devices suit better for gate schemes involving

Qubit	$E_{L,\alpha}/h$ (GHz)	$E_{C,\alpha}/h$ (GHz)	$E_{J,\alpha}/h$ (GHz)	$\omega_{01}^\alpha/2\pi$ (GHz)	$\omega_{12}^\alpha/2\pi$ (GHz)	$\omega_{03}^\alpha/2\pi$ (GHz)	$ \langle 0_\alpha \hat{n}_\alpha 1_\alpha \rangle $	$ \langle 1_\alpha \hat{n}_\alpha 2_\alpha \rangle $	$ \langle 0_\alpha \hat{n}_\alpha 3_\alpha \rangle $
A	1.09	1.06	4.62	0.53	3.80	7.03	0.14	0.58	0.41
B	1.88	1.03	5.05	1.02	3.75	8.25	0.22	0.63	0.32

TABLE I. Fluxonium parameters used for numerical simulations.

higher noncomputational levels because of larger n_{12}^α and n_{03}^α . In particular, single-qubit transition frequencies in the controlled- Z gate realization of Ref. [27], which was based on driving in proximity with the $|11\rangle - |21\rangle$ transition, were only 70 and 130 MHz.

In Figs. 2(a) and 2(b), we show both direct and cross matrix elements of \hat{n}_A and \hat{n}_B calculated numerically for parameters of Table I and $J_C/h = 350$ MHz. We make three main observations. First, we notice that direct charge matrix elements are large in comparison to cross matrix elements, e.g., $|\langle 00 | \hat{n}_A | 10 \rangle| \gg |\langle 00 | \hat{n}_B | 10 \rangle|$ in Fig. 2(a), since the cross matrix elements become nonzero only due to interaction-induced corrections, i.e., $\langle 00 | \hat{n}_B | 10 \rangle = 0$ when $J_C = 0$. Second, we notice, however, that the *change* of the matrix element with the qubit state changing is greater for cross matrix elements, e.g., $|\langle 10 | \hat{n}_B | 11 \rangle - \langle 00 | \hat{n}_B | 01 \rangle| < |\langle 10 | \hat{n}_A | 11 \rangle - \langle 00 | \hat{n}_A | 01 \rangle|$ in Fig. 2(b). This fact is in line with our previous reasoning that the interaction effects are linear in J_C in cross matrix elements and are quadratic in J_C in direct matrix elements. Finally, we also observe that $\Omega_{10-11} > \Omega_{01-11}$ since $|\langle 10 | \hat{n}_A | 11 \rangle - \langle 00 | \hat{n}_A | 01 \rangle| > |\langle 01 | \hat{n}_B | 11 \rangle - \langle 00 | \hat{n}_B | 10 \rangle|$. Therefore, we have chosen qubit B as the target qubit for parameters of Table I.

We find that magnitudes of cross matrix elements are well explained by an approximation based on first-order perturbation theory that accounts only for contributions coming from computational levels and from $|2k\rangle$, $|k2\rangle$, $|3k\rangle$, and $|k3\rangle$, where $k = 0, 1$. Analytic expressions for this approximation are derived in Appendix A. As an example, in Fig. 1(b), wavy lines show contributions to $\langle 10 | \hat{n}_A | 11 \rangle$ coming from various pairs of hybridized levels. We emphasize that in comparison to true two-level systems, here couplings to higher levels such as that between $|10\rangle$ and $|21\rangle$ are relevant and cannot be ignored. In fact, the dominant contributions to $\langle 10 | \hat{n}_A | 11 \rangle$ are coming from hybridization of $|10\rangle$ with $|21\rangle$ and of $|11\rangle$ with $|20\rangle$ rather than from hybridization of levels within the computational subspace. We also notice that because $\omega_{01}^A < \omega_{01}^B$, see Table I, all four contributions to $\langle 10 | \hat{n}_A | 11 \rangle$ interfere constructively, while, e.g., there is a destructive interference between contributions to $\langle 01 | \hat{n}_B | 11 \rangle$. In addition, since charge matrix elements for the qubit transition approximately scale with frequency, n_{01}^B is almost twice as large as n_{01}^A , which further increases contributions from hybridization of $|10\rangle$ and $|21\rangle$ and of $|11\rangle$ and $|20\rangle$ and eventually makes $\langle 10 | \hat{n}_A | 11 \rangle$ the largest cross matrix element among four of them, see Figs. 2(a) and 2(b).

D. Effective Hamiltonian

In this section, we use the language of effective Hamiltonian models [8, 20] to give a complementary perspective on gate operation. The effective Hamiltonian is restricted to the computational subspace, has a block-diagonal structure with respect to control-qubit states, is written in the appropriate rotating frame of two qubits, and describes an effective interaction induced by a microwave drive in addition to a static ZZ coupling. To focus on gate concept, we write it only to linear order in f , which yields

$$\hat{H}_{\text{eff}} = \frac{\xi_{ZX}}{2} \hat{\sigma}_z^A \otimes \hat{\sigma}_x^B + \frac{\xi_{IX}}{2} \hat{\sigma}_0^A \otimes \hat{\sigma}_x^B + \frac{\xi_{ZZ}}{4} \hat{\sigma}_z^A \otimes \hat{\sigma}_z^B. \quad (11)$$

Here ξ_{ZX} , ξ_{IX} , and ξ_{ZZ} are the rates of effective ZX , IX , and ZZ interactions, $\hat{\sigma}_0^A$ is the identity 2×2 matrix, and $\hat{\sigma}_i^\alpha$ with $i = x, z$ is the Pauli matrix for qubit α . It is ZX interaction that is essential for any gate based on the CR effect. For the SD gates, particularly, $\xi_{ZX} = \pm \xi_{IX}$. We note that even though we use tensor-product notation in Eq. (11), this Hamiltonian is written in the interacting (dressed) eigenbasis rather than in the basis of tensor-product noninteracting states.

To linear order in f , we find

$$\xi_{ZX} = f [\langle 00 | \hat{n}_A | 01 \rangle - \langle 10 | \hat{n}_A | 11 \rangle + \eta (\langle 00 | \hat{n}_B | 01 \rangle - \langle 10 | \hat{n}_B | 11 \rangle)], \quad (12a)$$

$$\xi_{IX} = f [\langle 00 | \hat{n}_A | 01 \rangle + \langle 10 | \hat{n}_A | 11 \rangle + \eta (\langle 00 | \hat{n}_B | 01 \rangle + \langle 10 | \hat{n}_B | 11 \rangle)], \quad (12b)$$

and

$$\xi_{ZZ} = \omega_{10-11} - \omega_{00-01}. \quad (12c)$$

If higher-order terms are properly taken into account, IX and ZX rates saturate with increasing the drive amplitude f , ZZ rates acquire small corrections, and two new terms - ZI and IZ - appear in Eq. (11) [19, 20]. The origin of the ZI term is AC Stark effect due to an off-resonance drive of the control qubit. While this effect is formally quadratic in f , its magnitude is relatively large because it is of zeroth order in J_C , so the induced ZI rate quickly becomes dominant in the effective Hamiltonian [20]. In comparison, IZ rate and f -dependent correction to ZZ rate are of higher order in both J_C and f and are rather small [20]. A possibly large magnitude of ZI rate is not relevant for gate operation as its effect

can be easily absorbed into virtual single-qubit Z rotations [37].

In Fig. 2(c), we plot ZX , IX , and ZZ rates calculated using perturbative Eqs. (12a)-(12c) as a function of the interaction strength J_C assuming only qubit A is driven, i.e., at $\eta = 0$. The drive amplitude f is chosen to correspond to $\lambda = 0.2$, where λ is the dimensionless drive amplitude for qubit A defined according to

$$\lambda = \frac{\Omega_{A,0}}{\Delta_{AB}}. \quad (13)$$

Here $\Omega_{A,0} = 2fn_{01}^A$ is the single-qubit resonance Rabi frequency for qubit A and $\Delta_{AB} = \omega_{01}^B - \omega_{01}^A$ is the detuning between qubit frequencies. The amplitude λ is a measure of the strength of the off-resonance Rabi oscillations of qubit A during the CR pulse; their contrast is given by $\lambda^2/(\lambda^2 + 1)$. Linear results of Eqs. (12a)-(12c) are valid under the condition $\lambda \ll 1$.

Figure 2(c) illustrates that the strengths of IX and ZX terms are comparable, which signifies the contribution of higher noncomputational levels into these rates. In comparison, in purely two-level models, $\xi_{IX} = 0$ [11, 20].

The SD variant of the CR scheme, Eq. 6, implies that $\xi_{IX} + \xi_{ZX} = 0$, which can be achieved by varying the drive amplitude of the second pulse applied to qubit B or parameter η . We illustrate this statement in Fig. 2(d) by plotting IX , ZX , and negative ZX rates vs η for the same λ as in Fig. 2(c) and the same J_C as in the top panels of Fig. 2. We observe that ξ_{ZX} is almost unaffected by changing η because the difference between two direct matrix elements in Eq. 12a is negligible as discussed in Sec. II C. In comparison, ξ_{IX} contains the sum of two direct matrix elements, so it strongly depends on η . In other words, a direct resonant drive of qubit B induces its rotation irrespective of state of qubit A , which is characterized by a change in ξ_{IX} .

E. Speed limit

In addition to activating controlled rotations of the target qubit, the CR drive (4) is applied off-resonantly to transitions of the control qubit, which contributes to coherent control errors and eventually limits gate speed. The simplest estimate for the maximum allowed drive amplitude of the CR drive can be found by equating the control-qubit effective drive amplitude given by $\Omega_{A,0}$ and drive detuning Δ_{AB} , which results in $\lambda \sim 1$, see Eq. (13). Then, using Eq. (9), we find the corresponding speed limit for the gate duration

$$t_{\text{fsl}} = \frac{n_{01}^A}{2|\langle 10|\hat{n}_A|11\rangle - \langle 00|\hat{n}_A|01\rangle|} \frac{2\pi}{\Delta_{AB}}, \quad (14)$$

which we refer to as the fundamental speed limit. A similar criteria based on the off-resonant drive of the control qubit but resulting in $\lambda \sim 1/2$ was used in Refs. [10, 17] to estimate the maximum possible gate rate. The detuning

between qubit frequencies Δ_{AB} is not restricted for small values for fluxoniums unlike transmons, where the choice of Δ_{AB} is often affected by the weak anharmonicity [19].

We note that Eq. (9) used to derive Eq. (14) is valid only in the limit of small λ . When terms of higher order in the drive amplitude are accounted for, Eq. (9) is modified and Ω_{10-11} saturates as a function of f at larger f [19]. Therefore, for $\lambda \sim 1$, the actual value of Ω_{10-11} is lower than that given by Eq. 9 and the corresponding gate is longer than t_{fsl} . In practice, experimentally implemented CR gates are typically at least three times the speed limit based on Eq. (14) modified for an appropriate system. Nevertheless, a quantum speed limit that is close to Eq. (14) was discovered numerically in the analysis of Ref. [18] for a system of coupled transmons with Eq. (14) modified for transmons. Close to that speed limit, however, very complex optimal-control pulses were necessary, which were found assuming unconstrained amplitude piecewise-constant controls with a high sampling rate of 0.1 ns.

In transmons, because of their weak anharmonicity, error due to coherent leakage into the $|1\rangle - |2\rangle$ transition of the control qubit can be significant and give an additional speed-limit restriction. Even though fluxoniums are strongly anharmonic, the corresponding charge matrix element n_{12}^{α} and thus the resonance Rabi frequency are typically a few times larger than those for the main $|0\rangle - |1\rangle$ transition, see Table I, which can still contribute to the coherent control error. To elaborate on this issue, we first define the dimensionless drive amplitude for the $|1_A\rangle - |2_A\rangle$ transition similarly to Eq. (13):

$$\lambda_{1-2} = \frac{\Omega_{A,0}^{12}}{\Delta_{AB}^{12}}. \quad (15)$$

Here $\Omega_{A,0}^{12} = 2fn_{12}^A$ and $\Delta_{AB}^{12} = \omega_{12}^A - \omega_{01}^B$ are the corresponding single-qubit resonance Rabi frequency and detuning between the transition and drive frequencies. For parameters of Table I, we find $\lambda_{1-2}/\lambda \approx 0.73 < 1$. Therefore, gate speed is primarily limited by the main $|0_A\rangle - |1_A\rangle$ transition of qubit A as discussed above, although leakage error can be comparable to the error due to rotation of the control qubit, see Sec. III B below for the discussion of error budget.

III. GATE FIDELITY

A. Unitary dynamics

In numerical simulations of gate dynamics, we use Gaussian envelopes

$$f(t) \propto \exp\left[-\frac{(t - t_{\text{gate}}/2)^2}{2\sigma^2}\right] - \exp\left[-\frac{(t_{\text{gate}}/2)^2}{2\sigma^2}\right] \quad (16)$$

for the microwave-drive term (4). Here t_{gate} is the gate duration, $0 < t < t_{\text{gate}}$, and $\sigma = t_{\text{gate}}/4$. We have verified

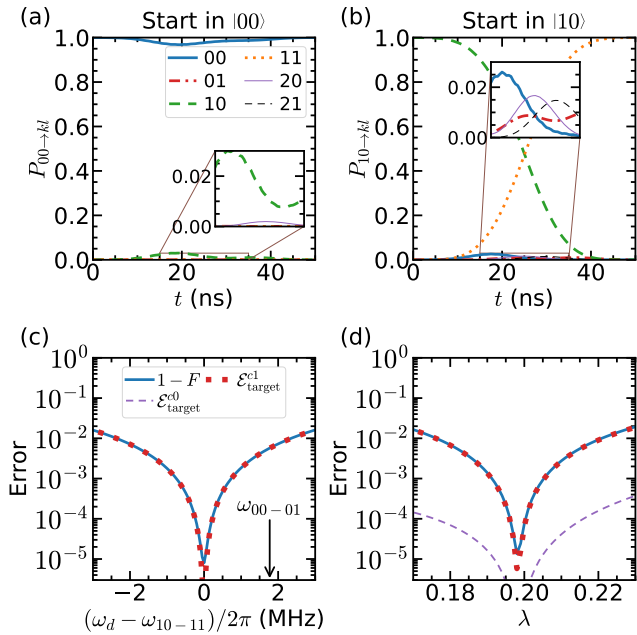


FIG. 3. (a), (b) Unitary time evolution of the populations of various two-qubit states during gate operation for the initial states $|00\rangle$ (a) and $|10\rangle$ (b). The gate is optimized over drive frequency and two drive amplitudes at fixed $J_C/h = 350$ MHz and $t_{\text{gate}} = 50$ ns, resulting in $F_{\text{coherent}} > 99.998\%$. (c), (d) Coherent gate error (blue solid lines) and target-rotation errors for control qubit in $|0\rangle$ (dashed purple lines) and in $|1\rangle$ (dotted red lines) vs drive frequency (c) and dimensionless drive amplitude (d) around their optimal values.

that substituting these envelopes with Gaussian flat-top pulses does not significantly affect gate error. For given pulse and other parameters, we first find the unitary evolution operator in the 25-levels Hilbert space composed of five levels coming from each qubit and then project it into the computational subspace to obtain a 4×4 matrix \hat{U}_{sim} . To compare it with the ideal CNOT operation defined by

$$\hat{U}_{\text{CNOT}} = \begin{pmatrix} 1 & 0 & 0 & 0 \\ 0 & 1 & 0 & 0 \\ 0 & 0 & 0 & 1 \\ 0 & 0 & 1 & 0 \end{pmatrix}, \quad (17)$$

we apply additional single-qubit Z rotations both before and after the gate, see Appendix B. In an experimental setting, such rotations can be performed instantly in software and do not contribute to gate error [37]. When \hat{U}_{sim} has the same amplitudes of matrix elements as \hat{U}_{CNOT} , these Z rotations reduce \hat{U}_{sim} to \hat{U}_{CNOT} exactly, so any phase error in \hat{U}_{sim} does not contribute to gate infidelity.

Let \hat{U} be the simulated gate operator \hat{U}_{sim} modified by the additional Z rotations. To calculate the coherent

gate fidelity, we use the standard expression [38]

$$F_{\text{coherent}} = \frac{\text{Tr}(\hat{U}^\dagger \hat{U}) + |\text{Tr}(\hat{U}_{\text{CNOT}}^\dagger \hat{U})|^2}{20}. \quad (18)$$

We optimize it numerically over the drive frequency, the overall drive amplitude, and the parameter η , see Eq. 4, which is equivalent to optimizing over the two drive amplitudes for drives applied to the control and target qubits. As starting values in the optimization procedure for a given t_{gate} , we use $\omega_d = \omega_{10-11}$, take η from Eq. (7), and calculate the overall amplitude prefactor from Eq. (9) assuming $\Omega_{10-11} = \pi/t_{\text{gate}}$ with an extra rescaling to account for the Gaussian pulse shape (16).

In Figs. 3(a) and 3(b), we illustrate such an optimized gate in time domain for $t_{\text{gate}} = 50$ ns and $J_C/h = 350$ MHz by plotting populations of several two-qubit states for two initial states. The coherent gate fidelity (18) for these parameters is greater than 99.998%. In insets, we show intermediate populations of some of the states that should have zero occupation probabilities in an ideal gate operation. Having $P_{00 \rightarrow 10} \neq 0$ in Fig. 3(a) and $P_{10 \rightarrow 00} \neq 0$ in Fig. 3(b), where $P_{kl \rightarrow k'l'}$ is the population of state $|k'l'\rangle$ for the initial state $|kl\rangle$, implies a small chance of spurious control-qubit rotations, and having $P_{10 \rightarrow 20} \neq 0$ and $P_{10 \rightarrow 21} \neq 0$ in Fig. 3(b) illustrates leakage to noncomputational states. We emphasize that all such control-qubit rotations and leakage probabilities are very small at the end of the pulse with a more detailed analysis of the error budget given in Sec. III B.

To check the stability of this optimized gate operation with respect to variations of pulse parameters, we plot the coherent gate error vs drive frequency detuning $\omega_d - \omega_{10-11}$ and vs dimensionless drive amplitude λ around their optimal values, see blue solid lines in Figs. 3(c) and 3(d). We observe that the coherent fidelity stays above 99.99% in the frequency window of about 500 kHz and in the drive-amplitude window of about 2% of the optimal drive amplitude, which is readily achievable in experiments.

We emphasize that the optimal value of ω_d is close to the frequency of the bright (driven) transition ω_{10-11} rather than to the frequency of the darkened transition ω_{00-01} , which is shown a vertical arrow in Fig. 3(c). This way, a controlled rotation of the target qubit is activated by an on-resonance drive, which reduces effects of static ZZ interaction (12c). To illustrate a high-fidelity gate in a system with strong ZZ , here we have chosen system parameters with a ZZ rate of $|\xi_{ZZ}|/2\pi \approx 2$ MHz, see the distance between ω_{10-11} and ω_{00-01} in Fig. 3(c). In comparison, in simpler schemes to implement a CR gate with a single CR drive followed by additional rotations of the target qubit [11], an ideal operation implies rotations of the target qubit for both states of the control. This condition is hard to achieve when static ZZ coupling is strong, which makes it impossible to drive the target qubit in resonance for both states of the control qubit. In this situation, the ZZ term can be mitigated by an echo

sequence [13–15, 21, 22], which increases gate duration. Therefore, the SD scheme has a definite advantage in systems with stronger ZZ . Another advantage of our technique is that the error due to extra dynamical phase induced by ZZ interaction does not contribute to gate infidelity because of additional single-qubit Z rotations both before and after the gate operation as described in Appendix B.

We next study coherent gate fidelity as a function of the pulse duration t_{gate} at fixed $J_C/h = 350$ MHz and as a function of J_C/h at fixed $t_{\text{gate}} = 50$ ns with the gate optimizations performed separately for each value of t_{gate} or J_C/h . The resulting error $1 - F_{\text{coherent}}$ is shown by the solid blue lines in Figs. 4 and 5, where parameters of Fig. 3 are indicated by squares and vertical arrows. We discuss the observed behavior of coherent error in more detail together with the error budget in Sec. III B.

B. Coherent error budget

Here we define several contributions to $1 - F_{\text{coherent}}$, relating them to those transition probabilities $P_{kl \rightarrow k'l'}(t_{\text{gate}})$ that should be zero for an ideal gate operation. For brevity, we omit the argument t_{gate} in these probabilities below. To derive the error-budget contributions, we first notice that $|\langle k'l' | \hat{U} | kl \rangle| = \sqrt{P_{kl \rightarrow k'l'}}$ when both states $|kl\rangle$ and $|k'l'\rangle$ are in the computational subspace. Then, we use Eq. (18) and the probability conservation law $\sum_{k'l'} P_{kl \rightarrow k'l'} = 1$, where the sum runs over all the two-qubit states, including noncomputational ones, to express $1 - F_{\text{coherent}}$ in terms of only those $P_{kl \rightarrow k'l'}$ that should be zero. Linearizing the resulting expression, we write

$$1 - F_{\text{coherent}} = \mathcal{E}_{\text{target}}^{c0} + \mathcal{E}_{\text{target}}^{c1} + \mathcal{E}_{\text{control}} + \mathcal{E}_{\text{leakage}} \quad (19)$$

with the individual terms explained below.

The first two terms of Eq. (19) represent the errors in the rotation of the target qubit for two states of the control qubit. When the control qubit is in its ground state, we have

$$\mathcal{E}_{\text{target}}^{c0} = \frac{1}{5} (P_{00 \rightarrow 01} + P_{01 \rightarrow 00}), \quad (20)$$

implying error due to rotation of the target qubit when it should remain idle. When the control qubit is in its state $|1\rangle$, we similarly find

$$\mathcal{E}_{\text{target}}^{c1} = \frac{1}{5} (P_{10 \rightarrow 10} + P_{11 \rightarrow 11}), \quad (21)$$

implying the error due to rotation of the target qubit on the Bloch sphere by an angle different from π . These two errors are shown by dashed purple and dotted red lines in Figs. 3(c), 3(d), 4, and 5. We observe that $\mathcal{E}_{\text{target}}^{c1}$ gives the dominant contribution to $1 - F_{\text{coherent}}$ when the pulse frequency or overall amplitude are slightly detuned from their optimal values, see Figs. 3(c) and 3(d).

At the same time, $\mathcal{E}_{\text{target}}^{c0}$ remains unimportant in these cases since the ratio of the two drive amplitudes is kept fixed, which enforces the SD condition (6). When η is also detuned from its optimal value (not shown in plots), the $|00\rangle - |01\rangle$ transition is no longer darkened, leading to a larger $\mathcal{E}_{\text{target}}^{c0}$. A small increase in $\mathcal{E}_{\text{target}}^{c0}$ with deviation of the drive amplitude λ in Fig. 3(d) is associated with nonlinear corrections, which are absent in the SD condition (6), but lead to a small change of the optimal η . For optimized pulses for a given t_{gate} , we find that $\mathcal{E}_{\text{target}}^{c0}$ and $\mathcal{E}_{\text{target}}^{c1}$ have similar values at short t_{gate} with their sum being the dominant contribution in $1 - F_{\text{coherent}}$, see Fig. 4. At long t_{gate} or large J_C/h , we find that $\mathcal{E}_{\text{target}}^{c1}$ increases and eventually determines $1 - F_{\text{coherent}}$.

The third term in Eq. (19) is the error due to transitions in the control qubit within the computational subspace:

$$\mathcal{E}_{\text{control}} = \frac{1}{5} \sum_{k,l,l'=0,1} P_{kl \rightarrow \bar{k}l'}, \quad (22)$$

where $\bar{0} = 1$ and vice versa. This error never dominates $1 - F_{\text{coherent}}$ for data points presented in this paper and is absent on the plots.

Finally, the last term in Eq. (19) describes the coherent leakage to higher noncomputational levels and is given by

$$\mathcal{E}_{\text{leakage}} = 1 - \frac{1}{4} \text{Tr}(\hat{U}^\dagger \hat{U}). \quad (23)$$

It is shown by green dash-dot lines in Figs. 4 and 5. This leakage error is the dominant contribution to $1 - F_{\text{coherent}}$ at intermediate t_{gate} and is the reason of its local minimum at $t_{\text{gate}} \approx 32$ ns. We observe that $\mathcal{E}_{\text{target}}^{c0}$, $\mathcal{E}_{\text{target}}^{c1}$, and $\mathcal{E}_{\text{leakage}}$ have discontinuities as a function of J_C/h at $J_C/h \approx 210$ and ≈ 240 MHz, which is accompanied by kinks in $1 - F_{\text{coherent}}$, see Fig. 5. This behaviour is explained by the crossing of different local minima of $1 - F_{\text{coherent}}$ at these values of J_C/h . A different optimization protocol, e.g., the one that minimizes $\mathcal{E}_{\text{leakage}}$ rather than $1 - F_{\text{coherent}}$, can result in smoother behavior of the total error.

We notice that $1 - F_{\text{coherent}}$ vs t_{gate} in Fig. 4 crosses the 0.01 threshold at around 27 ns. At the same time, the fundamental speed limit (14) is less than 10 ns for these parameters, which can be easily understood by noticing that $\lambda \lesssim 0.2$ at $t_{\text{gate}} = 50$ ns, see Fig. 3(d), and that Eq. (14) is based on the $\lambda \sim 1$ criterion. This discrepancy between the shortest possible t_{gate} in a realistic gate and t_{fsl} given by Eq. (14) is in line with our previous reasoning based on effects that are nonlinear in the drive amplitude, see text below Eq. (14). To approach the limit given by Eq. (14), optimal-control pulses, which have more complicated shapes than the Gaussian envelope (16), are necessary [18].

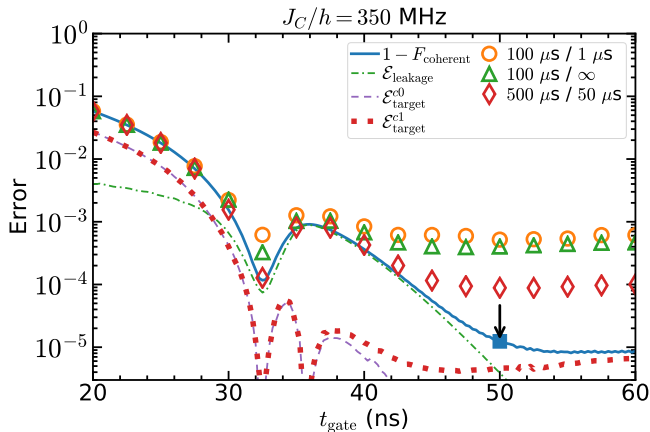


FIG. 4. Gate error vs t_{gate} at $J_C/h = 350$ MHz with pulse parameters optimized for each value of t_{gate} . Lines show the total coherent error (blue solid line), leakage error (green dash-dot line), and target-qubit rotation errors for the control qubit in states $|0\rangle$ (purple dashed line) and in $|1\rangle$ (red dotted line). The square marker and vertical arrow point at the parameters of Figs. 3(a) and 3(b). Empty markers show gate error in the presence of relaxation processes and relaxation-limited dephasing for $T_1^{0-1} = 100 \mu\text{s}$ and $T_1^{1-2} = 1 \mu\text{s}$ (circles), for $T_1^{0-1} = 100 \mu\text{s}$ and $T_1^{1-2} = \infty$ (triangles), and for $T_1^{0-1} = 500 \mu\text{s}$ and $T_1^{1-2} = 50 \mu\text{s}$ (diamonds).

C. Dissipation effects

To complete our analysis of gate operation, we discuss the error due to incoherent effects. We focus on qubit relaxation processes and assume that they give the dominant contribution to the loss of coherence, resulting in $T_2 = 2T_1$ relation for the coherence (T_2) and relaxation (T_1) times of all the relevant transitions. Since the system is mostly staying in the computational subspace with only small intermediate excitation of qubit second excited states, see Figs. 3(a) and 3(b), the dominant error is expected to come from incoherent effects in $|0_\alpha\rangle - |1_\alpha\rangle$ transitions of both qubits. We denote the corresponding relaxation time by T_1^{0-1} with the assumption that it is the same in both qubits. Because the lifetime of the second excited states can be much shorter than T_1^{0-1} , we also account for the relaxation in $|1_\alpha\rangle - |2_\alpha\rangle$ transitions with the corresponding time T_1^{1-2} for both qubits. We follow the procedure outlined in Ref. [31] to simulate gate dynamics by solving the full master equation, to find the resulting 16×16 χ matrix, and then to calculate gate fidelity by comparing this matrix to its ideal value. We implement this procedure for pulse parameters that are optimized for coherent error (18).

We first consider a suboptimal value $T_1^{0-1} = 100 \mu\text{s}$ for the main qubit transitions and a very short relaxation time $T_1^{1-2} = 1 \mu\text{s}$ of the $|1_\alpha\rangle - |2_\alpha\rangle$ transitions. We find that these parameters still result in gate error below 10^{-3} for most of the data points, see circles in Figs. 4 and 5. To estimate the contribution of relaxation specifically

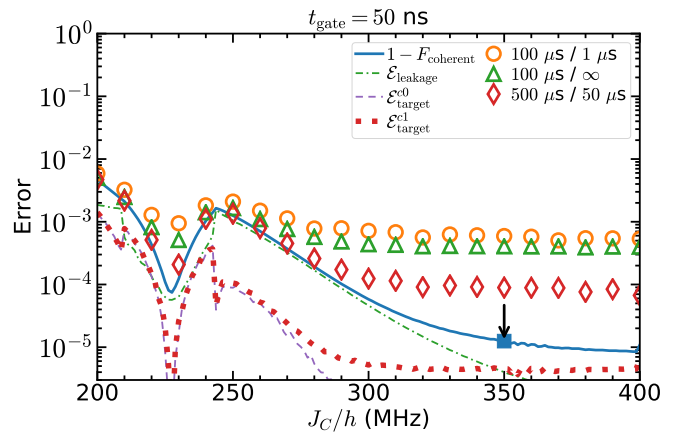


FIG. 5. Gate error vs J_C/h at $t_{\text{gate}} = 50$ ns with pulse parameters optimized for each value of J_C/h . Lines show the total coherent error (blue solid line), leakage error (green dash-dot line), and target-qubit rotation errors for the control qubit in states $|0\rangle$ (purple dashed line) and in $|1\rangle$ (red dotted line). The square marker and vertical arrow point at the parameters of Figs. 3(a) and 3(b). Empty markers show gate error in the presence of relaxation processes and relaxation-limited dephasing for $T_1^{0-1} = 100 \mu\text{s}$ and $T_1^{1-2} = 1 \mu\text{s}$ (circles), for $T_1^{0-1} = 100 \mu\text{s}$ and $T_1^{1-2} = \infty$ (triangles), and for $T_1^{0-1} = 500 \mu\text{s}$ and $T_1^{1-2} = 50 \mu\text{s}$ (diamonds).

in $|0_\alpha\rangle - |1_\alpha\rangle$ transitions, we then remove the collapse operators corresponding to the $|2_\alpha\rangle - |1_\alpha\rangle$ relaxation from the master equation and compare the two results. We find that gate error for simulations without relaxation in $|1_\alpha\rangle - |2_\alpha\rangle$ transitions is slightly smaller, see triangles in Figs. 4 and 5 labeled as $T_1^{1-2} = \infty$. Even though T_1^{1-2} is only $1 \mu\text{s}$, the contribution of relaxation in $|1_\alpha\rangle - |2_\alpha\rangle$ transitions to gate error is below 0.1%, which agrees with very low excitation probability of noncomputational states during the gate operation, see Figs. 3(a) and 3(b). Finally, we present the results for devices with $T_1^{0-1} = 500 \mu\text{s}$ and $T_1^{1-2} = 50 \mu\text{s}$, see diamond-shape markers in Figs. 4 and 5. These longer relaxation times, which are realistically achievable in modern fluxonium devices [25, 26], reduce gate error down to 10^{-4} values.

IV. CONCLUSIONS

In conclusion, we have investigated a microwave-activated two-qubit gate scheme for fluxonium circuits, which is based on selective darkening of a transition in the computational subspace [10, 17]. The scheme is facilitated by the cross-resonance effect [8, 9, 11] and leads to high-fidelity CNOT gates even for strong ZZ coupling and large detuning between qubit frequencies. The gate fidelity in excess of 99.99% evaluated for the unitary dynamics is achievable for a basic shape of the microwave radiation and does not require complicated pulse sequences or special arrangement of qubit energy levels.

The population of higher excited states remains low during gate pulses, so the gate performance is nearly unaffected by the relaxation processes from energy levels outside of the computational subspace. Even for a short lifetime of $1 \mu\text{s}$ of the second excited state, the contribution to the gate error remains below 0.1%.

The optimized gate operation was analyzed in this paper for a device with a relatively strong ZZ coupling, which was $\xi_{ZZ}/2\pi \approx 2 \text{ MHz}$ in the case discussed in Fig. 3. This example illustrates an excellent resilience of the SD gates against spurious ZZ coupling. While this specific CNOT gate works well for this value of ξ_{ZZ} , it is generally preferred to have processors with much smaller values of the ZZ crosstalk during single-qubit gates and while idling. The magnitude of ZZ coupling can be greatly reduced by applying an always-on off-resonance microwave drive, which was demonstrated for fluxoniums [28] and transmons [7, 39]. Additional techniques to mitigate this crosstalk are based on using a multipath coupling scheme [5, 40] and/or a tunable coupler [40, 41], which will likely become an ultimate scalable solution for a multiqubit processor. Without such techniques, for fluxonium parameters used in our analysis, a 50 ns-long high-fidelity gate is possible for a smaller value of J_C/h with $\xi_{ZZ}/2\pi < 1 \text{ MHz}$, see Fig. 5. Because gate rate (9) scales with J_C linearly, while ξ_{ZZ} is quadratic in J_C , an additional reduction of J_C/h by a factor of 2 increases t_{gate} to 100 ns, but reduces ξ_{ZZ} by an extra factor of 4. We also note that here we have performed a very basic optimization procedure of microwave pulses, which can be greatly improved with optimal control to allow a fast gate with even smaller J_C/h or ξ_{ZZ} .

In transmons, the rate of the cross-resonance gate is maximized when two qubits are in the straddling regime, so the detuning between qubit frequencies is smaller than their anharmonicity [19]. In addition, in a multiqubit transmon processor, an extra care is required to tune frequencies to reduce spectator errors [21]. These requirements of simultaneously having small detunings and avoiding frequency collisions, including transitions to the second excited states, lead to a complicated frequency-allocation procedure for transmon-based processors [42]. Modern fabrication techniques result in 1% imprecision in transmon frequencies [43], which is insufficient to obtain a high yield of devices that satisfy frequency conditions unless an additional postfabrication tuning is performed [44, 45].

In comparison, frequency requirements for fluxoniums are much less stringent, which guarantees a better fabrication yield of fluxonium-based processors. The road map for a scalable fluxonium-based processor, including frequency allocation and estimates for the fabrication yield, has been recently presented in Ref. [46]. There, it was argued that the two-qubit gate realized via the CR

effect is a viable solution for a scalable design for such a processor. In addition, it was shown that a combination of capacitive and inductive couplings can effectively suppress the static ZZ rate, while maintaining high-fidelity CR gates.

Finally, another attractive feature of the fluxonium is that its low frequency implies a long coherence time, which currently exceeds 1 ms in best devices [26]. We have shown that comparable qubit lifetimes together with realistic relaxation time of $50 \mu\text{s}$ of the second excited states result in gate error within the 10^{-4} range. We note that the fluxonium frequency in Ref. [26] was 163 MHz, while devices with higher qubit frequencies are preferred for the realization of a high-fidelity SD scheme to increase hybridization of qubit states in a system with capacitive coupling. Thus, simulations in this paper were performed for two qubits with frequencies in the 500 MHz – 1 GHz range. Generally, higher-frequency fluxoniums have proportionally lower coherence times. However, much less community effort has been devoted to improving fluxonium devices in comparison to transmons. In particular, suboptimal fabrication procedure and antenna design were used in high-coherence fluxonium devices of Refs. [25, 26], resulting in effective dielectric loss tangents that are an order of magnitude larger than in the best 3D transmons [47]. Given recent advances in materials and fabrications of 2D transmons [48, 49], the fluxonium coherence time can be pushed up significantly both in planar and 3D geometries. These arguments indicate that the fluxonium is an excellent candidate for a scalable processor, and the SD gate scheme is suitable for its realization.

ACKNOWLEDGMENTS

We would like to thank Long Nguyen, Quentin Ficheux, Haonan Xiong, Loïck Le Guevel, Ebru Dogan, and Dario Rosenstock for stimulating discussions. We acknowledge the support from ARO-LPS HiPS program (grant No. W911NF-18-1-0146). V.E.M. and M.G.V acknowledge the Faculty Research Award from Google and fruitful conversations with the members of the Google Quantum AI team. We used the QuTiP software package [50, 51] and performed computations using resources and assistance of the UW-Madison Center For High Throughput Computing (CHTC) in the Department of Computer Sciences. The CHTC is supported by UW-Madison, the Advanced Computing Initiative, the Wisconsin Alumni Research Foundation, the Wisconsin Institutes for Discovery, and the National Science Founda-

Appendix A: Perturbation theory

Here we develop approximate expressions for the cross matrix elements of the charge operators based on first-order perturbation theory. Among an infinite number of all the contributions that are formally linear in J_C , we aim at keeping only those whose magnitude is not very small. To this end, we truncate the Hilbert space and account only for contributions coming from hybridization within the computational subspace and only with those noncomputational levels where one of the qubits is in its second or third excited states. We first define

$$\hbar V_{kl,k'l'} = \langle kk' | \hat{V} | ll' \rangle = J_C n_{kl}^A n_{k'l'}^B, \quad (\text{A1})$$

where

$$n_{kl}^\alpha = -i \langle k_\alpha | \hat{n}_\alpha | l_\alpha \rangle. \quad (\text{A2})$$

Keeping only relevant terms, we find

$$|00\rangle \approx |0_A\rangle|0_B\rangle - \frac{V_{11,00}}{\omega_{01}^A + \omega_{01}^B} |1_A\rangle|1_B\rangle - \frac{V_{31,00}}{\omega_{03}^A + \omega_{01}^B} |3_A\rangle|1_B\rangle - \frac{V_{13,00}}{\omega_{01}^A + \omega_{03}^B} |1_A\rangle|3_B\rangle + \dots, \quad (\text{A3a})$$

$$|11\rangle \approx |1_A\rangle|1_B\rangle + \frac{V_{00,11}}{\omega_{01}^A + \omega_{01}^B} |0_A\rangle|0_B\rangle - \frac{V_{20,11}}{\omega_{12}^A - \omega_{01}^B} |2_A\rangle|0_B\rangle + \frac{V_{02,11}}{\omega_{01}^A - \omega_{12}^B} |0_A\rangle|2_B\rangle + \dots, \quad (\text{A3b})$$

$$|01\rangle \approx |0_A\rangle|1_B\rangle - \frac{V_{10,01}}{\omega_{01}^A - \omega_{01}^B} |1_A\rangle|0_B\rangle - \frac{V_{12,01}}{\omega_{01}^A + \omega_{12}^B} |1_A\rangle|2_B\rangle - \frac{V_{30,01}}{\omega_{03}^A - \omega_{01}^B} |3_A\rangle|0_B\rangle + \dots, \quad (\text{A3c})$$

and

$$|10\rangle \approx |1_A\rangle|0_B\rangle + \frac{V_{01,10}}{\omega_{01}^A - \omega_{01}^B} |0_A\rangle|1_B\rangle - \frac{V_{21,10}}{\omega_{12}^A + \omega_{01}^B} |2_A\rangle|1_B\rangle + \frac{V_{03,10}}{\omega_{01}^A - \omega_{03}^B} |0_A\rangle|3_B\rangle + \dots \quad (\text{A3d})$$

Therefore, we find the following expressions for the cross matrix elements of \hat{n}_A (e.g., for transitions of qubit B):

$$\langle 00 | \hat{n}_A | 01 \rangle \approx -2i \frac{J_C}{\hbar} n_{01}^B \left[\frac{(n_{01}^A)^2 \omega_{01}^A}{(\omega_{01}^A)^2 - (\omega_{01}^B)^2} + \frac{(n_{03}^A)^2 \omega_{03}^A}{(\omega_{03}^A)^2 - (\omega_{01}^B)^2} \right] \quad (\text{A4a})$$

and

$$\langle 10 | \hat{n}_A | 11 \rangle \approx 2i \frac{J_C}{\hbar} n_{01}^B \left[\frac{(n_{01}^A)^2 \omega_{01}^A}{(\omega_{01}^A)^2 - (\omega_{01}^B)^2} - \frac{(n_{12}^A)^2 \omega_{12}^A}{(\omega_{12}^A)^2 - (\omega_{01}^B)^2} \right]. \quad (\text{A4b})$$

Similarly, for \hat{n}_B we find

$$\langle 00 | \hat{n}_B | 10 \rangle \approx 2i \frac{J_C}{\hbar} n_{01}^A \left[\frac{(n_{01}^B)^2 \omega_{01}^B}{(\omega_{01}^A)^2 - (\omega_{01}^B)^2} + \frac{(n_{03}^B)^2 \omega_{03}^B}{(\omega_{01}^A)^2 - (\omega_{03}^B)^2} \right] \quad (\text{A5a})$$

and

$$\langle 01 | \hat{n}_B | 11 \rangle \approx -2i \frac{J_C}{\hbar} n_{01}^A \left[\frac{(n_{01}^B)^2 \omega_{01}^B}{(\omega_{01}^A)^2 - (\omega_{01}^B)^2} - \frac{(n_{12}^B)^2 \omega_{12}^B}{(\omega_{01}^A)^2 - (\omega_{12}^B)^2} \right]. \quad (\text{A5b})$$

Appendix B: Single-qubit Z rotations

An evolution operator projected into the computational subspace has the form

$$\hat{U}_{\text{sim}} = \begin{pmatrix} X e^{i\phi_{00}} & x & x & x \\ x & X e^{i\phi_{01}} & x & x \\ x & x & x & X e^{i\phi_a} \\ x & x & X e^{i\phi_b} & x \end{pmatrix}, \quad (\text{B1})$$

where X stands for absolute values of matrix elements that are equal to 1 in the ideal operator and x is used to describe the remaining elements. To compare this operator with the ideal one, we use additional single-qubit Z rotations both *before and after* the gate operation. Namely,

$$\hat{U}_{\text{sim}} \rightarrow \hat{U} = e^{-i\phi_{00}} \begin{pmatrix} 1 & 0 & 0 & 0 \\ 0 & e^{i\phi_1} & 0 & 0 \\ 0 & 0 & e^{i\phi_2} & 0 \\ 0 & 0 & 0 & e^{i(\phi_1+\phi_2)} \end{pmatrix} \begin{pmatrix} X e^{i\phi_{00}} & x & x & x \\ x & X e^{i\phi_{01}} & x & x \\ x & x & x & X e^{i\phi_a} \\ x & x & X e^{i\phi_b} & x \end{pmatrix} \begin{pmatrix} 1 & 0 & 0 & 0 \\ 0 & e^{i\phi_3} & 0 & 0 \\ 0 & 0 & 1 & 0 \\ 0 & 0 & 0 & e^{i\phi_3} \end{pmatrix}. \quad (\text{B2})$$

Thus, before the gate operation, we perform additional Z rotation on the target qubit only (phase ϕ_3), while rotations on both target and control are applied after the operation. The phases determining these three rotations are given by

$$\begin{cases} \phi_1 = \frac{1}{2}(-\phi_{01} + \phi_a - \phi_b + \phi_{00}), \\ \phi_2 = \frac{1}{2}(\phi_{01} - \phi_a - \phi_b + \phi_{00}), \\ \phi_3 = \frac{1}{2}(-\phi_{01} - \phi_a + \phi_b + \phi_{00}), \end{cases} \quad (\text{B3})$$

which nullifies all the phases of important matrix elements (labeled by X).

-
- [1] M. H. Devoret and R. J. Schoelkopf, Superconducting Circuits for Quantum Information: An Outlook, *Science* **339**, 1169 (2013).
- [2] G. Wendin, Quantum information processing with superconducting circuits: a review, *Rep. Prog. Phys.* **80**, 106001 (2017).
- [3] M. Kjaergaard, M. E. Schwartz, J. Braumüller, P. Krantz, J. I-J Wang, S. Gustavsson, and W. D. Oliver, Superconducting Qubits: Current State of Play, *Annu. Rev. Condens. Matter Phys.* **11**, 369 (2020).
- [4] Y. Sung, L. Ding, J. Braumüller, A. Vepsäläinen, B. Kannan, M. Kjaergaard, A. Greene, G. O. Samach, C. McNally, D. Kim, A. Melville, B. M. Niedzielski, M. E. Schwartz, J. L. Yoder, T. P. Orlando, S. Gustavsson, and W. D. Oliver, Realization of High-Fidelity CZ and ZZ-Free iSWAP Gates with a Tunable Coupler, *Phys. Rev. X* **11**, 021058 (2021).
- [5] A. Kandala, K. X. Wei, S. Srinivasan, E. Magesan, S. Carnevale, G. A. Keefe, D. Klaus, O. Dial, and D. C. McKay, Demonstration of a High-Fidelity cnot Gate for Fixed-Frequency Transmons with Engineered ZZ Suppression, *Phys. Rev. Lett.* **127**, 130501 (2021).
- [6] V. Negirneac, H. Ali, N. Muthusubramanian, F. Battistel, R. Sagastizabal, M. S. Moreira, J. F. Marques, W. J. Vlothuizen, M. Beekman, C. Zachariadis, N. Haider, A. Bruno, and L. DiCarlo, High-Fidelity Controlled- Z Gate with Maximal Intermediate Leakage Operating at the Speed Limit in a Superconducting Quantum Processor, *Phys. Rev. Lett.* **126**, 220502 (2021).
- [7] K. X. Wei, E. Magesan, I. Lauer, S. Srinivasan, D. F. Bogorin, S. Carnevale, G. A. Keefe, Y. Kim, D. Klaus, W. Landers, N. Sundaresan, C. Wang, E. J. Zhang, M. Steffen, O. E. Dial, D. C. McKay, and A. Kandala, Hamiltonian Engineering with Multicolor Drives for Fast Entangling Gates and Quantum Crosstalk Cancellation, *Phys. Rev. Lett.* **129**, 060501 (2022).
- [8] G. S. Paraoanu, Microwave-induced coupling of superconducting qubits, *Phys. Rev. B* **74**, 140504 (2006).
- [9] C. Rigetti and M. Devoret, Fully microwave-tunable universal gates in superconducting qubits with linear couplings and fixed transition frequencies, *Phys. Rev. B* **81**, 134507 (2010).
- [10] P. C. de Groot, J. Lisenfeld, R. N. Schouten, S. Ashhab, A. Lupaşcu, C. J. P. M. Harmans, and J. E. Mooij, Selective darkening of degenerate transitions demonstrated with two superconducting quantum bits, *Nat. Phys.* **6**, 763 (2010).
- [11] J. M. Chow, A. D. Córcoles, J. M. Gambetta, C. Rigetti, B. R. Johnson, J. A. Smolin, J. R. Rozen, G. A. Keefe, M. B. Rothwell, M. B. Ketchen, and M. Steffen, Simple All-Microwave Entangling Gate for Fixed-Frequency Superconducting Qubits, *Phys. Rev. Lett.* **107**, 080502 (2011).
- [12] J. M. Chow, J. M. Gambetta, A. D. Córcoles, S. T. Merkel, J. A. Smolin, C. Rigetti, S. Poletto, G. A. Keefe, M. B. Rothwell, J. R. Rozen, M. B. Ketchen, and M. Steffen, Universal Quantum Gate Set Approaching Fault-Tolerant Thresholds with Superconducting Qubits, *Phys. Rev. Lett.* **109**, 060501 (2012).
- [13] A. D. Córcoles, J. M. Gambetta, J. M. Chow, J. A. Smolin, M. Ware, J. Strand, B. L. T. Plourde, and M. Steffen, Process verification of two-qubit quantum gates by randomized benchmarking, *Phys. Rev. A* **87**, 030301 (2013).
- [14] M. Takita, A. D. Córcoles, E. Magesan, B. Abdo, M. Brink, A. Cross, J. M. Chow, and J. M. Gambetta, Demonstration of Weight-Four Parity Measurements in the Surface Code Architecture, *Phys. Rev. Lett.* **117**, 210505 (2016).
- [15] S. Sheldon, E. Magesan, J. M. Chow, and J. M. Gambetta, Procedure for systematically tuning up cross-talk in the cross-resonance gate, *Phys. Rev. A* **93**, 060302 (2016).
- [16] P. Jurcevic, A. Javadi-Abhari, L. S. Bishop, I. Lauer, D. F. Bogorin, M. Brink, L. Capelluto, O. Günliük, T. Itoko, N. Kanazawa, A. Kandala, G. A. Keefe, K. Kr-

- sulich, W. Landers, E. P. Lewandowski, D. T. McClure, G. Nannicini, A. Narasgond, H. M. Nayfeh, E. Pritchett, M. B. Rothwell, S. Srinivasan, N. Sundaresan, C. Wang, K. X. Wei, C. J. Wood, J.-B. Yau, E. J. Zhang, O. E. Dial, J. M. Chow, and J. M. Gambetta, Demonstration of quantum volume 64 on a superconducting quantum computing system, *Quantum Sci. Technol.* **6**, 025020 (2021).
- [17] P. C. de Groot, S. Ashhab, A. Lupaşcu, L. DiCarlo, F. Nori, C. J. P. M. Harmans, and J. E. Mooij, Selective darkening of degenerate transitions for implementing quantum controlled-NOT gates, *New J. Phys.* **14**, 073038 (2012).
- [18] S. Kirchhoff, T. Keßler, P. J. Liebermann, E. Assémat, S. Machnes, F. Motzoi, and F. K. Wilhelm, Optimized cross-resonance gate for coupled transmon systems, *Phys. Rev. A* **97**, 042348 (2018).
- [19] V. Tripathi, M. Khezri, and A. N. Korotkov, Operation and intrinsic error budget of a two-qubit cross-resonance gate, *Phys. Rev. A* **100**, 012301 (2019).
- [20] E. Magesan and J. M. Gambetta, Effective Hamiltonian models of the cross-resonance gate, *Phys. Rev. A* **101**, 052308 (2020).
- [21] N. Sundaresan, I. Lauer, E. Pritchett, E. Magesan, P. Jurcevic, and J. M. Gambetta, Reducing Unitary and Spectator Errors in Cross Resonance with Optimized Rotary Echoes, *PRX Quantum* **1**, 020318 (2020).
- [22] M. Malekakhlagh, E. Magesan, and D. C. McKay, First-principles analysis of cross-resonance gate operation, *Phys. Rev. A* **102**, 042605 (2020).
- [23] M. Malekakhlagh and E. Magesan, Mitigating off-resonant error in the cross-resonance gate, *Phys. Rev. A* **105**, 012602 (2022).
- [24] V. E. Manucharyan, E. Boaknin, M. Metcalfe, R. Vijay, I. Siddiqi, and M. Devoret, Microwave bifurcation of a Josephson junction: Embedding-circuit requirements, *Phys. Rev. B* **76**, 014524 (2007).
- [25] L. B. Nguyen, Y.-H. Lin, A. Somoroff, R. Mencia, N. Grabon, and V. E. Manucharyan, High-Coherence Fluxonium Qubit, *Phys. Rev. X* **9**, 041041 (2019).
- [26] A. Somoroff, Q. Ficheux, R. A. Mencia, H. Xiong, R. Kuzmin, and V. E. Manucharyan, Millisecond coherence in a superconducting qubit, *arXiv:2103.08578* (2021).
- [27] Q. Ficheux, L. B. Nguyen, A. Somoroff, H. Xiong, K. N. Nesterov, M. G. Vavilov, and V. E. Manucharyan, Fast Logic with Slow Qubits: Microwave-Activated Controlled-Z Gate on Low-Frequency Fluxoniums, *Phys. Rev. X* **11**, 021026 (2021).
- [28] H. Xiong, Q. Ficheux, A. Somoroff, L. B. Nguyen, E. Dogan, D. Rosenstock, C. Wang, K. N. Nesterov, M. G. Vavilov, and V. E. Manucharyan, Arbitrary controlled-phase gate on fluxonium qubits using differential ac Stark shifts, *Phys. Rev. Research* **4**, 023040 (2022).
- [29] K. N. Nesterov, I. V. Pechenezhskiy, C. Wang, V. E. Manucharyan, and M. G. Vavilov, Microwave-activated controlled-Z gate for fixed-frequency fluxonium qubits, *Phys. Rev. A* **98**, 030301 (2018).
- [30] M. Abdelhafez, B. Baker, A. Gyenis, P. Mundada, A. A. Houck, D. Schuster, and J. Koch, Universal gates for protected superconducting qubits using optimal control, *Phys. Rev. A* **101**, 022321 (2020).
- [31] K. N. Nesterov, Q. Ficheux, V. E. Manucharyan, and M. G. Vavilov, Proposal for Entangling Gates on Fluxonium Qubits via a Two-Photon Transition, *PRX Quantum* **2**, 020345 (2021).
- [32] H. Zhang, S. Chakram, T. Roy, N. Earnest, Y. Lu, Z. Huang, D. K. Weiss, J. Koch, and D. I. Schuster, Universal Fast-Flux Control of a Coherent, Low-Frequency Qubit, *Phys. Rev. X* **11**, 011010 (2021).
- [33] Y. Chen, K. N. Nesterov, V. E. Manucharyan, and M. G. Vavilov, Fast Flux Entangling Gate for Fluxonium Circuits, *Phys. Rev. Applied* **18**, 034027 (2022).
- [34] F. Bao, H. Deng, D. Ding, R. Gao, X. Gao, C. Huang, X. Jiang, H.-S. Ku, Z. Li, X. Ma, X. Ni, J. Qin, Z. Song, H. Sun, C. Tang, T. Wang, F. Wu, T. Xia, W. Yu, F. Zhang, G. Zhang, X. Zhang, J. Zhou, X. Zhu, Y. Shi, J. Chen, H.-H. Zhao, and C. Deng, Fluxonium: An Alternative Qubit Platform for High-Fidelity Operations, *Phys. Rev. Lett.* **129**, 010502 (2022).
- [35] I. N. Moskalenko, I. S. Besedin, I. A. Simakov, and A. V. Ustinov, Tunable coupling scheme for implementing two-qubit gates on fluxonium qubits, *Appl. Phys. Lett.* **119**, 194001 (2021).
- [36] E. Dogan, D. Rosenstock, L. Lořick, L. Guevel, H. Xiong, R. A. Mencia, A. Somoroff, K. N. Nesterov, M. G. Vavilov, V. E. Manucharyan, and C. Wang, Demonstration of the Two-Fluxonium Cross-Resonance Gate, *arXiv:2204.11829* (2022).
- [37] D. C. McKay, C. J. Wood, S. Sheldon, J. M. Chow, and J. M. Gambetta, Efficient Z gates for quantum computing, *Phys. Rev. A* **96**, 022330 (2017).
- [38] L. H. Pedersen, N. M. Møller, and K. Mølmer, Fidelity of quantum operations, *Phys. Lett. A* **367**, 47 (2007).
- [39] B. K. Mitchell, R. K. Naik, A. Morvan, A. Hashim, J. M. Kreikebaum, B. Marinelli, W. Lavrijsen, K. Nowrouzi, D. I. Santiago, and I. Siddiqi, Hardware-Efficient Microwave-Activated Tunable Coupling between Superconducting Qubits, *Phys. Rev. Lett.* **127**, 200502 (2021).
- [40] P. Mundada, G. Zhang, T. Hazard, and A. Houck, Suppression of Qubit Crosstalk in a Tunable Coupling Superconducting Circuit, *Phys. Rev. Applied* **12**, 054023 (2019).
- [41] F. Yan, P. Krantz, Y. Sung, M. Kjaergaard, D. L. Campbell, T. P. Orlando, S. Gustavsson, and W. D. Oliver, Tunable Coupling Scheme for Implementing High-Fidelity Two-Qubit Gates, *Phys. Rev. Applied* **10**, 54062 (2018).
- [42] A. Morvan, L. Chen, J. M. Larson, D. I. Santiago, and I. Siddiqi, Optimizing frequency allocation for fixed-frequency superconducting quantum processors, *Phys. Rev. Research* **4**, 023079 (2022).
- [43] J. M. Kreikebaum, K. P. O'Brien, A. Morvan, and I. Siddiqi, Improving wafer-scale Josephson junction resistance variation in superconducting quantum coherent circuits, *Supercond. Sci. Technol.* **33**, 06LT02 (2020).
- [44] E. J. Zhang, S. Srinivasan, N. Sundaresan, D. F. Bogorin, Y. Martin, J. B. Hertzberg, J. Timmerwilke, E. J. Pritchett, J.-B. Yau, C. Wang, W. Landers, E. P. Lewandowski, A. Narasgond, S. Rosenblatt, G. A. Keefe, I. Lauer, M. B. Rothwell, D. T. McClure, O. E. Dial, J. S. Orcutt, M. Brink, and J. M. Chow, High-performance superconducting quantum processors via laser annealing of transmon qubits, *Sci. Adv.* **8**, eabi6690 (2022).
- [45] J. B. Hertzberg, E. J. Zhang, S. Rosenblatt, E. Magesan, J. A. Smolin, J.-B. Yau, V. P. Adiga, M. Sandberg, M. Brink, J. M. Chow, and J. S. Orcutt, Laser-annealing Josephson junctions for yielding scaled-up superconducting quantum processors, *npj Quantum Inf.* **7**, 129 (2021).

- [46] L. B. Nguyen, G. Koolstra, Y. Kim, A. Morvan, T. Chistolini, S. Singh, K. N. Nesterov, C. Jünger, L. Chen, Z. Pedramrazi, B. K. Mitchell, J. M. Kreikebaum, S. Puri, D. I. Santiago, and I. Siddiqi, Blueprint for a High-Performance Fluxonium Quantum Processor, *PRX Quantum* **3**, 037001 (2022).
- [47] C. Wang, C. Axline, Y. Y. Gao, T. Brecht, Y. Chu, L. Frunzio, M. H. Devoret, and R. J. Schoelkopf, Surface participation and dielectric loss in superconducting qubits, *Appl. Phys. Lett.* **107**, 162601 (2015).
- [48] A. P. M. Place, L. V. H. Rodgers, P. Mundada, B. M. Smitham, M. Fitzpatrick, Z. Leng, A. Premkumar, J. Bryon, A. Vrajitoarea, S. Sussman, G. Cheng, T. Madhavan, H. K. Babla, X. H. Le, Y. Gang, B. Jäck, A. Gye-nis, N. Yao, R. J. Cava, N. P. de Leon, and A. A. Houck, New material platform for superconducting transmon qubits with coherence times exceeding 0.3 milliseconds, *Nat. Commun.* **12**, 1779 (2021).
- [49] C. Wang, X. Li, H. Xu, Z. Li, J. Wang, Z. Yang, Z. Mi, X. Liang, T. Su, C. Yang, G. Wang, W. Wang, Y. Li, M. Chen, C. Li, K. Linghu, J. Han, Y. Zhang, Y. Feng, Y. Song, T. Ma, J. Zhang, R. Wang, P. Zhao, W. Liu, G. Xue, Y. Jin, and H. Yu, Towards practical quantum computers: transmon qubit with a lifetime approaching 0.5 milliseconds, *npj Quantum Inf.* **8**, 3 (2022).
- [50] J. R. Johansson, P. D. Nation, and F. Nori, QuTiP: An open-source Python framework for the dynamics of open quantum systems, *Comp. Phys. Comm.* **183**, 1760 (2012).
- [51] J. R. Johansson, P. D. Nation, and F. Nori, QuTiP 2: A Python framework for the dynamics of open quantum systems, *Comp. Phys. Comm.* **184**, 1234 (2013).